Ab initio calculations of the electronic and optical properties of germanium selenide

2007 J. Phys.: Condens. Matter 19 186211

(http://iopscience.iop.org/0953-8984/19/18/186211)

IOP PUBLISHING JOURNAL OF PHYSICS: CONDENSED MATTER

J. Phys.: Condens. Matter **19** (2007) 186211 (24pp) doi:10.1088/0953-8984/19/18/186211

Ab initio calculations of the electronic and optical properties of germanium selenide

L Makinistian[1] **and E A Albanesi**[1,2]

[1] Facultad de Ingeniería, Universidad Nacional de Entre Ríos, 3101 Oro Verde (ER), Argentina
[2] INTEC-CONICET, Güemes 3450, 3000 Santa Fe, Argentina

E-mail: lmakinistian@ceride.gov.ar and eaa@intec.ceride.gov.ar

Received 27 December 2006, in final form 15 March 2007
Published 5 April 2007
Online at stacks.iop.org/JPhysCM/19/186211

Abstract

We have performed an *ab initio* calculation of the germanium selenide electronic structure, adopting the LDA and GGA approximations for the exchange–correlation potential within the DFT. These calculations have been carried out with and without the inclusion of the spin–orbit interaction. The subtle changes it produces in the band structure, the density of states and the optical properties have been discussed. Also, we propose the s-Ge state contribution at the edge of the valence band as having an important role. Based on our electronic structure, we discuss germanium selenide experimental core spectra and optical properties. We found excellent agreement between our results and available experimental core spectra data, and our calculated optical functions of GeSe explain the origin of the optical transitions, comparing them satisfactorily against existing experimental data.

1. Introduction

The IV–VI compounds are used in the manufacture of cut-off devices, photovoltaic cells and infrared lasers [1–3] and detectors. Also, they have been studied for the evaluation of nanostructure etching [4]. Among these compounds, the black phosphorus structured GeS, GeSe, SnSe and SnS present very interesting features.

In this work, we present results on GeSe, which (along with GeS, SnSe and SnS) has an orthorhombic structure and belongs to the *Pnma* 62 (D_{2h}^{16}) space group. Its lattice parameters are $a = 10.862$ Å, $b = 3.862$ Å and $c = 4.414$ Å, and correspond to the $\Gamma \rightarrow X$, $\Gamma \rightarrow Y$ and $\Gamma \rightarrow Z$ directions in the first Brillouin zone (BZ) (figures 1 and 2), respectively. The unit cell contains eight atoms organized in two adjacent double layers that are perpendicular to the direction of the a-axis. The atoms in each double layer bond to their three nearest neighbours by covalent bonds and form a zigzag chain along the direction of the minor axis of the crystal (figure 1). As a consequence of the dominant van der Waals character of the bonds between

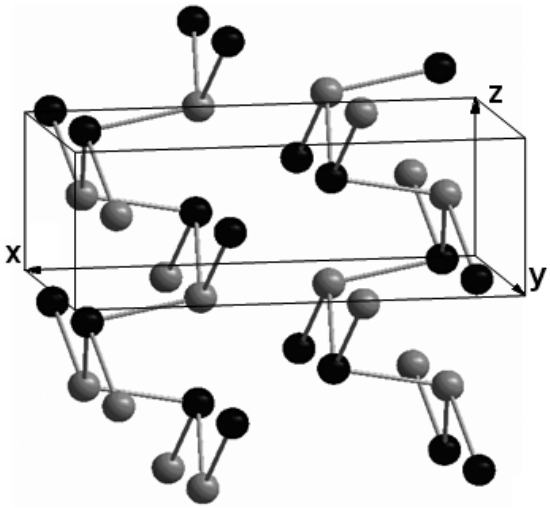

Figure 1. The *Pnma* 62 orthorhombic structure of GeSe.

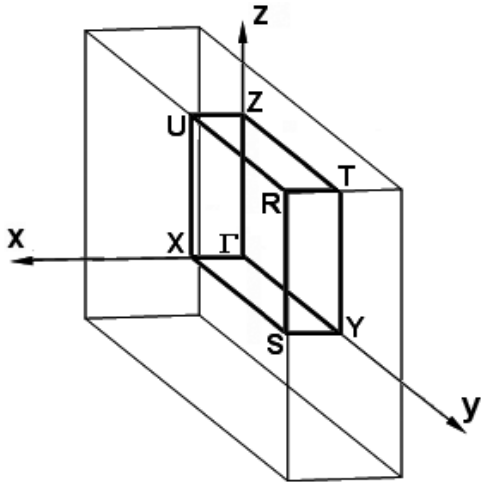

Figure 2. The Brillouin zone, with axes x, y and z corresponding to the crystal axes a, b and c, respectively.

adjacent layers, this material cleaves easily along the b–c [100] planes. The GeSe has an interesting intermediate behaviour between a two-and a three-dimensional material.

During the past decades, several studies on the IV–VI chalcogenides have been performed. Among them, although both cubic and orthorhombic ones were experimentally and theoretically studied, the orthorhombic ones were less extensively assessed and, therefore, understood. Moreover, their structural anisotropy brought about experimental and theoretical difficulties which have prevented a full agreement among different publications [5].

As to previous experimental work on GeSe, the following studies have been carried out: photoemission [6, 7], high resolution electron energy loss (HREELS) [8], transmittance [9], reflectance [10, 11], thermoreflectance [10], refraction index [12], photoconductivity [13], photoelectron partial-yield and constant-initial-state (CIS) spectra [14] and x-ray powder

diffraction plus Raman spectroscopy (for structural, vibrational and electronic properties related to compression mechanisms) [15]. Owing to the fact that the GeSe compound is quite stable at room temperature (since its melting point is about 780 °C, and it remains in the orthorhombic structure up to a pressure of 82 GPa [16]), most of these experiments were performed about, though below, room temperature. Regarding theoretical calculations, only a few have been performed: with the pseudopotential method (PM) [10, 15], and with the linear combination of atomic orbitals method (LCAO) [17].

State-of-the-art calculations have sensibly improved, so that an exhaustive and updated theoretical study of GeSe band structure, electronic density of states (DOS) and optical properties based on *ab initio* calculations is quite desirable. Most of the previous calculations were performed within the framework of semiempirical approaches, or involving simplifications such as spin–orbit coupling neglect, which made calculations easier and less demanding of computational time. The disadvantage of these methods is that there are parameters that must be fitted to experiments. Therefore, although they accomplish a general coincidence with experimentalists, the differences can lead to different interpretations of the experimental data. In fact, we show how our exhaustive treatment of hybridization allows a notable agreement with experiments, compared with less satisfactory results such as those obtained with the LCAO method (see section 3.1). We discuss the location and nature (direct or indirect) of the bandgap and the influence of the spin–orbit interaction, gathering and integrating previous results found in theoretical and experimental publications.

2. Calculation method

We have modelled the GeSe using a full potential linearized augmented plane wave (FP-LAPW) method [18–24], within the density functional theory (DFT) [25–27]. In this work, we used the WIEN2k package [28], which self-consistently finds the eigenvalues and eigenfunctions of the Kohn–Sham [29] equations for the system, using an R_{MT} of 2.40 (for both Ge and Se), an $l_{\max}$ of 10 and a $R_{\mathrm{MT}} \cdot K_{\max}$ product of 8 (implying a plane wave expansion cut-off of $\sim$ 11.1 Ryd). As part of our approach, we have used the local density approximation (LDA), in the Perdew–Wang parametrization [30], for the exchange and correlation potential. This approximation has had great success in dealing with the calculation of electronic properties. However, as is well known, it does not accurately describe some important properties, for example, by underestimating the bandgaps. A formal correction is achieved by including the gradient of the charge density. This is the so-called generalized gradient approximation (GGA) [30, 31], which we have used in the formal Perdew–Burke–Ernzerhof (PBE) parametrization scheme [32–34]. This corrected functional is semi-local and thus more sensitive to non-spherical components of the density. It could result in a better performance when applied in a full potential scheme like the one implemented in the WIEN2k package. In spite of this general behaviour of both approximations, and taking as the reference the GGA results, we find that the LDA errors on the bandgap and the band-structure determination are remarkably small for GeSe.

It is to be emphasized, though, that both LDA and GGA always yield underestimated bandgaps. An usual empirical correction of this is the scissors operator [35], which basically consists of adjusting the bandgap with a constant potential to reproduce the experimental energy bandgaps. This operator is often used, particularly in the determination of the bandgap offsets [36, 37] which appear when considering interfaces between different semiconductors, and also when optical transitions are studied [38]. We have applied it, with a value of 0.38 eV, to all our results: band structures and densities of states (by shifting the conduction regions up), and optical properties.

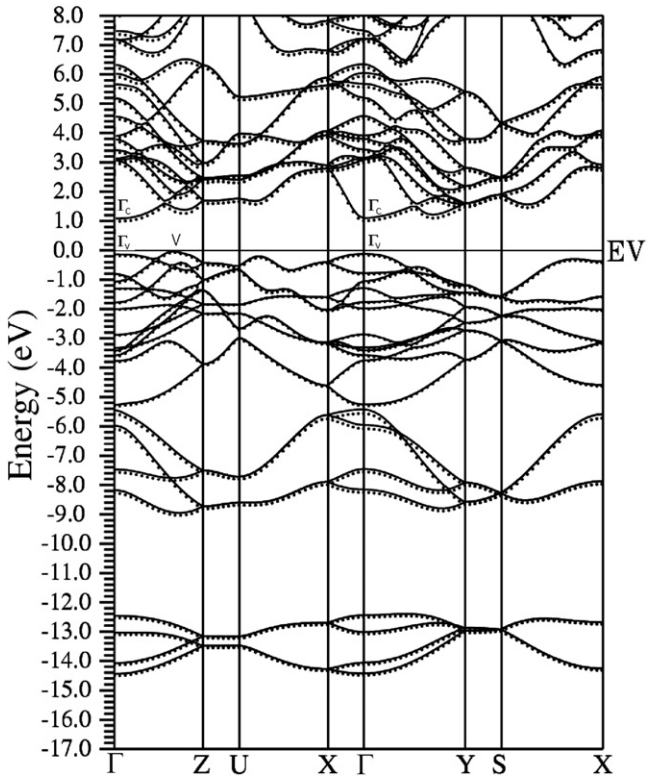

Figure 3. Band structure with LDA (dots) and GGA (lines), both without the spin–orbit interaction.

The calculation of optical properties begins with a good selfconsistent electronic structure. This is a key requisite since the calculation of optical functions involves matrix elements from the momentum operator, and the eigenfunctions used in their calculation must be precise. The inclusion of the spin–orbit interaction yields more peaks and with their energies better established. Since the present scheme is a very accurate one, our calculations give good account of the non-rigid shifts appearing in the conduction band energies of semiconductors.

3. Discussion of results

3.1. Band structure, DOS and core spectra

Figure 3 shows there is no sensible difference between the band structures predicted by LDA and GGA approaches for GeSe.

The main features of the electronic structure can be followed. Between −14.52 and −12.37 eV a group of bands mainly corresponding to the 4s-Se level can be seen. A bundle of bands originated from the 4s-Ge level and a minor contribution of the 4p-Se level are seen between −9.03 and −5.38 eV. These are followed at the region closer to the Fermi energy (E_F), which extends from −5.38 up to 0 eV, by a group of bands formed by the hybridization of 4p-Ge and 4p-Se levels with a contribution of the 4s-Ge level toward the lower binding energies. With regards to the conduction band, it mainly results from the hybridization of 4p-Ge and 4p-Se, with minor contributions of 4s-Ge atomic orbitals (towards the least excited

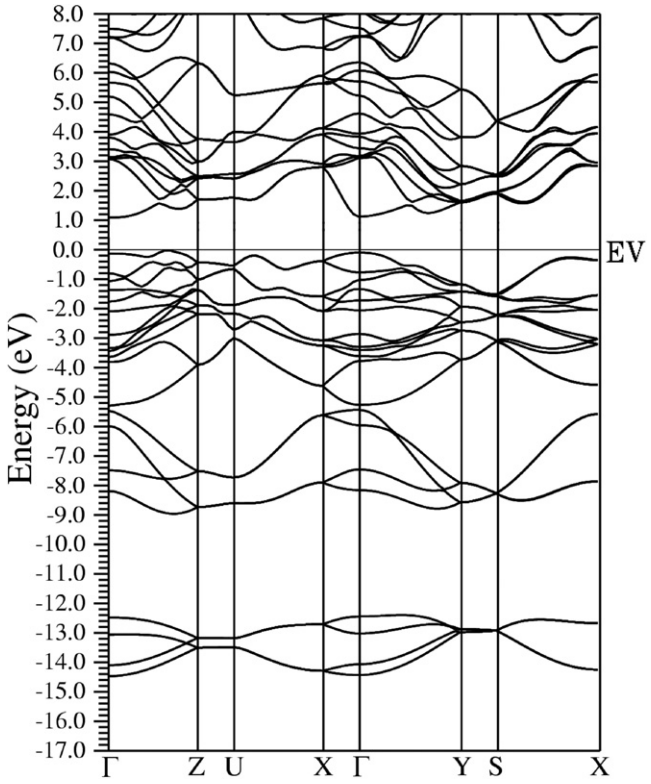

Figure 4. Band structure with GGA, with the spin–orbit interaction.

states) and of 4d levels of Ge and Se from 6.42 eV up, approximately. Several degrees of degeneracy are observed in the different directions of the first BZ: in the $\Gamma \rightarrow Z, X \rightarrow \Gamma$ and $\Gamma \rightarrow Y$ directions, 20 non-degenerated bands, except for the spin, are filled with the 40 valence electrons (16 corresponding to the Ge and 24 to the Se); the $Z \rightarrow U, U \rightarrow X$ and $Y \rightarrow S$ directions present ten bands with double degeneracy; and the S point (at the edge of the BZ) shows five values of energies with a fourfold degeneracy.

As to the spin–orbit coupling, figures 3 and 4 show some subtle differences introduced by this interaction in the upper part of the valence band (along the whole k-path except the $Y \rightarrow S$ direction). A splitting of bands is seen below the top of the valence band and in the bottom part of the conduction band along the $S \rightarrow X$ direction. The DOS allows us to identify this splitting as corresponding to $4p_x$, $4p_y$-Se and $4p_x$-Ge for the valence and conduction bands, respectively. Spin–orbit coupling also introduces several slight changes of shape in other bands in the same range of energies, and some splitting is also observed in the $Z \rightarrow U$ and $U \rightarrow X$ directions.

It should be mentioned that the bands over the $\Gamma \rightarrow X$ line (corresponding to the largest lattice parameter, i.e. to the axis perpendicular to the cleavage plane of the crystal) indicate a strong decrease of the charge carriers' mobility for the lowest energies of the conduction band and the highest of the valence band, in concordance with the strong anisotropy of the system in this direction.

The total and partial (s, p and d atomic orbitals) densities of states obtained in this work are shown in figure 5. It can be seen that they are in agreement with the **e** description of the band

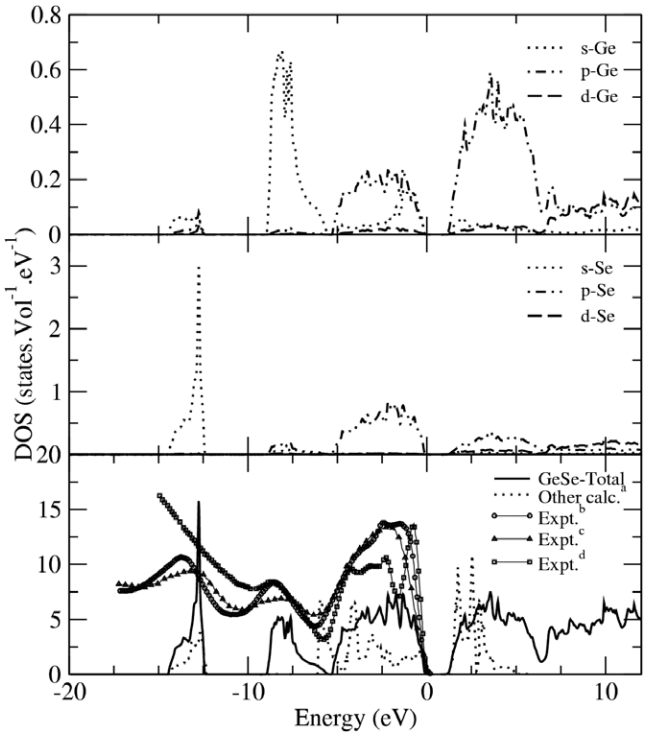

Figure 5. DOS of the s, p and d orbitals of the Ge and the Se. Total density: our calculation, other calculation [a] [17] and experimental results, [b] [7], [c] [6], [d] [14].

structure, which presents three well defined regions below E_F. Also in this figure, our total DOS calculated with the GGA with spin–orbit interaction is compared against experimental curves obtained with photoemission measurements [6, 7] and against the result of the only previous DOS calculations, made with the LCAO method [17]. When comparing DOS curves, it is usual to take as reference the zero at the top of the valence band. However, one of the difficulties encountered in photoemission measurements is to precisely determine reference energies, since the broadening tails going through zero appear not very well defined. Thus, we have chosen to align the sharp edge closer to the Fermi level (corresponding to the 4s, p-Ge and 4p-Se orbitals), tending to avoid this problem. As regards the locations of the main structures of the DOS, ours correlate very satisfactorily with those of the experimental curves. In fact, the curve of [14] presents a fine structure of the valence band that clearly resembles our calculation (in particular, their deep valley at −1.65 eV, to be compared with ours at −1.50 eV).

The DOS calculated with the LCAO method shows differences with the other curves as much in the energy positions, as in the valence band widths (except for the 4s-Se structure between −14.52 and −12.37 eV, which clearly coincides). This is mainly due to the fact that the LCAO calculation was implemented with interactions only between nearest neighbours. This implementation presents the drawback of not making a good description of hybridization. As a consequence, the bands and DOS appear quite decoupled (i.e., there is less overlapping among the different contributions than in our calculations), thus exaggerating the layered structure of the material.

The enhanced description of hybridization that our calculations perform has strong consequences, and our band structure and DOS sensibly differ from the ones published by

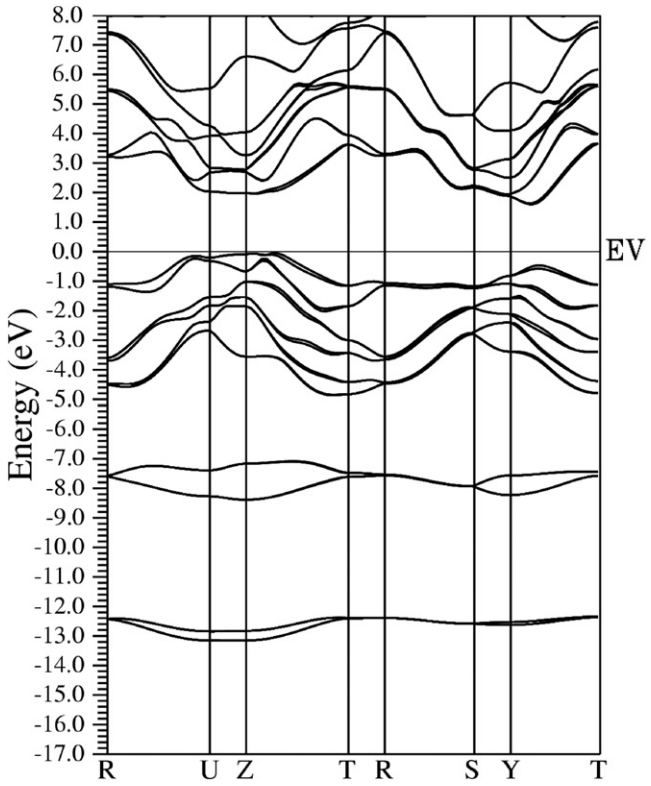

Figure 6. Our *ab initio* calculated band structure, with GGA and including spin–orbit interaction, in less symmetrical directions in the BZ.

Gashimzade [17]. However, they are similar to those of Valiukonis *et al* [10], which were calculated with the pseudopotential method. In spite of the resemblance, there are clear differences: (a) their bands seem to be stretched downwards by approximately 2 eV, so that their bands at the top of the valence bands are slightly less hybridized than ours; and (b) since they neglect the spin–orbit interaction, a discussion of the splitting of bands in various directions of the BZ is absent.

To stress this point, we can remark from figure 4 that the directions involving the Γ point, which is the most symmetrical region in the BZ, are the most hybridized. Thus, these are the regions where the spreading and crossing of bands is increased. The Z → U → S and Y → S directions are, instead, less symmetrical and hybridization decreases. In figure 6 we plot the band structure in the planes R → U → Z → T and R → S → Y → T, showing that only in these special regions the material becomes rather decoupled (i.e., less hybridized), obtaining for the less symmetrical direction, which is the R → S edge, the most decoupled bands. The material as a whole, however, maintains the hybridization as the important key in building these physical properties, mainly determined by the morphology of the top and bottom parts of the valence and conduction bands, respectively.

At the bottom of figure 5, our calculated total DOS is compared with three experimental ones [6, 7, 14] and with another calculation [17]. It can be seen that, while our calculation, along with those of Kemeny *et al* [7] and Taniguchi *et al* [14], presents a fine structure of the valence band top structure (from −5.38 eV up to 0 eV), the result of Shalvoy *et al* [6] does

Table 1. Relevant calculated DOS peaks and their contributing states.

		Contributing states	
DOS peak	DOS energy	Main	Minor
v_9	−8.27	s-Ge	p-Se
v_8	−7.71	s-Ge	p_x, p_y-Se
v_7	−4.70	p-Se	p-Ge
v_6	−3.80	p_x, p_y, p_z-Se	p_z, p_x, p_y-Ge
v_5	−3.59	p_x, p_y, p_z-Se	p_x, p_y, p_z-Ge
v_4	−2.63	p_z, p_x, p_y-Se	p_z, p_x, p_y-Ge
v_3	−1.71	p_z, p_x, p_y-Se	p_x, p_y, p_z-Ge
v_2	−1.31	p_z, p_x, p_y-Se	p_x, p_y, p_z-Ge
v_1	−0.69	p_x, p_y, p_z-Se	p_y, p_x, p_z-Ge, s-Ge
VBM	0	p_x, p_y-Se, s-Ge	p_z-Se
c_1	1.64	p-Ge	p-Se
A–B	1.93	p_z, p_x-Ge	p-Se
A′–B′	2.15	p_x, p_z-Ge	p_z-Ge, p-Se
c_2	2.93	p_x-Ge	p_y, p_z-Ge, p-Se
b–b′	3.16	p_x-Ge	p_y, p_z-Ge, p-Se
c_3	3.54	p_z, p_x, p_y-Ge	p-Se
c_4	4.00	p_z, p_x, p_y-Ge	p_z, p_x, p_y-Se
c_5	4.60	p_z, p_y, p_x-Ge	p-Se
c	5.88	p-Ge	p-Se

not. We believe this is most likely due to the fact that Shalvoy *et al* worked with polycrystalline samples, unlike the other experimentalists, who used single crystals. Also, our calculated curve for this region shows that an important s-cation state contribution is present at the top of the valence band, a contribution that has not been reported so far. More specifically, our results show that this region is mostly formed by the hybridization of the stronger 4p-Se levels with the 4p-Ge, but also by the narrower 4s-Ge levels appearing at the edge of the valence bands, which strongly contribute to the valence band maximum (VBM) formation (see figure 5, first floor). We assign the presence of these s-cation states, hybridized with the p-cation and p-anion contributions, as the most important feature in defining most physical properties (since they shape the behaviour of the maximum that determines the bandgap). This had already been found to be the key in the bandgap formation in the cubic IV–VI compounds [39–41], and consequently in the physical properties of those materials. The resemblance of the physical properties of orthorhombic IV–VI materials among themselves is also well established [6, 14]. Therefore, based on the aforesaid, in spite of being aware of the differences between cubic and orthorhombic IV–VI compounds, we suggest this behaviour of the s-cation states at the edge of the valence band as the fingerprint of the IV–VI compounds, that any description should achieve in order to accurately describe this family of compounds.

In order to facilitate the following discussions, in table 1 we present the composition of the peaks v_1–v_9 in the valence bands of the DOS as they are shown in figure 7, in terms of state type, and the kind of atom from which they are originated. We have also included in this table the same information with respect to the main peaks, named A–B, A′–B′, c_1, c_2, c_3, c_4, c_5 and c of the conduction band DOS.

With regards to the energy bandgap, our calculations show that it is indirect, and that is located in the line $\Gamma \rightarrow Z$, going from the point V to Γ_C (see figure 3). Our gap, calculated with the inclusion of the spin–orbit coupling, is 1.08 eV (interestingly, the calculation without

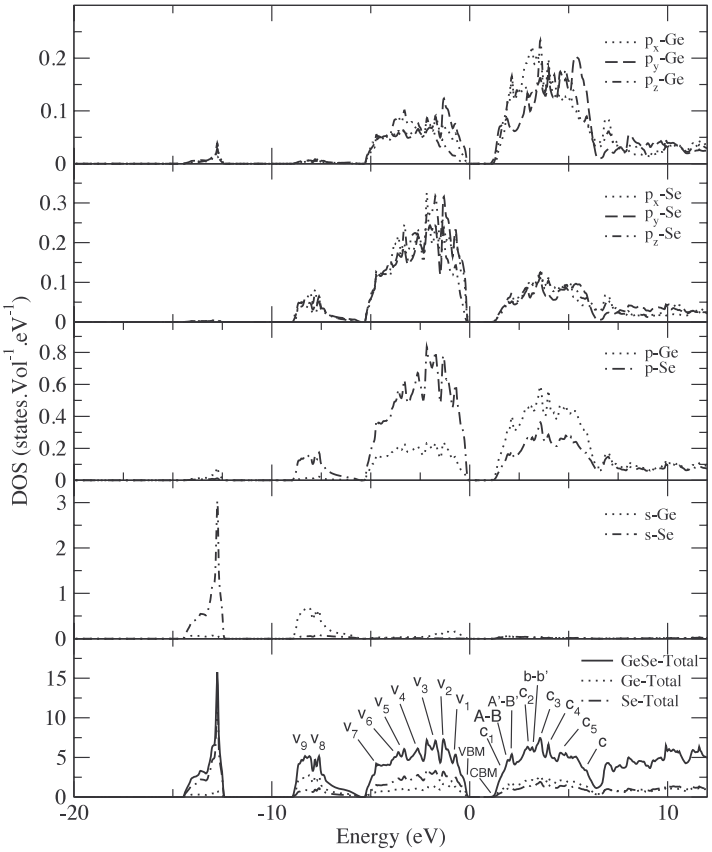

Figure 7. Density of the states of the p_x, p_y and p_z orbitals of the Ge and the Se.

the inclusion of the spin–orbit coupling yields a gap of 1.05 eV, lower than that with). The direct gap on $\Gamma(\Gamma_V \rightarrow \Gamma_C)$ is 1.18 eV (1.20 eV without spin–orbit coupling), which is slightly higher than indirect, but does not need the extra momentum of a phonon for the occurrence of a transition.

As to the DOS calculated to discriminate the contribution of the different p orbitals (p_x, p_y and p_z) (see figure 7), it indicates a higher probability of transitions from the p_x and p_y levels than from the p_z levels. Table 2 shows a summary of our bandgaps (with and without spin–orbit coupling) and others found in the literature (experimental and theoretical).

By measuring the partial-yield spectra of GeSe, Taniguchi *et al* [14] studied the absorption spectrum in the core excitation region, for the electric field parallel to *c* (called *a* in their paper) and *b* axes, $\vec{E} \parallel c$ and $\vec{E} \parallel b$, respectively. They associated it with the interaction of the 3d-Ge core levels (cation spectra) and the 3d-Se core levels (anion spectra) with the conduction bands.

It is known that both LDA and GGA are inaccurate in estimating the bandgaps (by underestimating them), and the 3d core levels (yielding values 1–4 eV higher than the experimental ones). In order to improve these inaccuracies, new techniques based on two particle operators and capable of incorporating excitons to the absorption spectra description (still built upon the DFT framework) are being developed [38, 42]. Moreover, given the fact that DFT is a ground state formalism, the description of the excited states in the conduction band could be enhanced [43, 44]. Therefore, and taking into account that some experimental

Table 2. Experimental and theoretical values of the GeSe energy bandgap. Values are in eV.

	Theoretical	
Experimental	Our calculations	Other calculations
1.07[a]		
1.075 ± 0.017 for the c-axis (their a-axis) and 1.080 ± 0.016 for the b-axis (their c-axis)[b]	1.08 indirect in $\Gamma \rightarrow Z$ (V to Γ_c), with spin–orbit coupling	1.50 direct in $\Gamma \rightarrow Z$[d] at $\frac{3}{4}$ from Γ
1.144 ± 0.011 for the c-axis (their a-axis) and 1.167 ± 0.025 for the b-axis (their c-axis)[c]	1.05 indirect in $\Gamma \rightarrow Z$ (V to Γ_c), without spin–orbit coupling	1.45 indirect in $\Gamma \rightarrow Z$[e] at $\frac{3}{4}$ from Γ
1.29[d]		

[a] Reference [9].
[b] Reference [11]. Transmission and reflectivity measurements at room temperature.
[c] Reference [13]. Photoconductivity measurements at room temperature.
[d] Reference [17].
[e] Reference [10].

discrepancies persist [14], we suggest that a thorough study of the excitonic effect on GeSe is worth undertaking. However, these procedures involve a huge amount of calculation, and can be performed at a few special k-points where the excitonic effects seem to be important.

We show how our results on the conduction bands are qualitatively and quantitatively compatible with their measurements. We can use the experimental values for both the bandgap and the measured Ge $3d_{5/2}$ and Ge $3d_{3/2}$ multiplets to explain, through interaction with the conduction band, the core absorption spectrum. The experimental values [14] from core-level photoemission measurement added to the experimental bandgap energy give 30.55 and 31.09 eV for the Ge $3d_{5/2}$ and the Ge $3d_{3/2}$ states, respectively. Taniguchi *et al* [14] found these two main peaks, each of them with a double structure. The first double structure corresponds to Ge $3d_{5/2}$, and its two peaks, called A and B, occur at 30.56 and 30.77 eV for $\vec{E} \parallel c$, and at 30.55 and 30.69 eV for $\vec{E} \parallel b$, respectively. The second double structure corresponds to Ge $3d_{3/2}$, with its two peaks called A′ and B′, located at 31.18 and 31.39 eV for $\vec{E} \parallel c$, and at 31.18 and 31.36 eV for $\vec{E} \parallel b$, respectively.

We can explain the A–B and A′–B′ structures as originated from a cooperative effect produced by relatively flat bands in different regions of the BZ. The first structure, A–B, shown in our DOS conduction band in figure 7, comes mainly from the first single, flat, conduction bands in the directions $Z \rightarrow U$, the first one-third of $U \rightarrow X$, $Y \rightarrow S$, the first half of $S \rightarrow X$, and the first one-third of $Y \rightarrow T$, together with the rest of the mixed bands about that energy in the whole BZ. The second structure, A′–B′, comes mainly from the second, flat conduction bands in the directions $Z \rightarrow U$, the last one-third of $U \rightarrow X$, $X \rightarrow \Gamma$, $Y \rightarrow S$, and the last one-third of $S \rightarrow X$. All mentioned contributions, together with the rest of the mixed bands about each energy in the *whole* BZ, give the well resolved peaks shown as A–B and A′–B′ in our conduction band DOS of figure 7. The first peak is at 1.93, 0.85 eV above the CBM, while the second peak is, also well defined, at 2.15, 1.07 eV above the CBM. These give our theoretical fine structure A–B and A′–B′ splitting of 0.22 eV (0.19 eV if spin–orbit interaction is not included, A–B and A′–B′ almost at the same locations), to be compared with the 0.21 eV (for both A–B and A′–B′) for the experimental $\vec{E} \parallel c$ measurement; and the 0.14 and 0.18 eV, for A–B and A′–B′, respectively, for the experimental $\vec{E} \parallel b$ measurement.

In GeSe, the spin–orbit splitting of the 3d-Se core level is about 0.85 eV [14]. Taniguchi *et al* [14] have measured the partial-yield spectra for the Se $3d_{5/2}$ and Se $3d_{3/2}$ core doublet,

for $\vec{E} \parallel c$, and $\vec{E} \parallel b$, obtaining five broad structures at 55.0, 55.9, 56.2, 57.0, and 59.0 eV, for $\vec{E} \parallel c$, and 55.0, 55.9, 56.2, 57.1, and 59.1 eV, for $\vec{E} \parallel b$, naming them a, a′, b, b′ and c, respectively. They assigned the structures a–a′ and b–b′ to the 3d-Se core level spin–orbit doublet, since splitting energies are about the same (0.90 and 0.80 eV of a–a′ and b–b′, against 0.85 eV of the core level spin–orbit splitting). Their peaks a, b and c appear about 0.6, 1.8 and 4.6 eV for $\vec{E} \parallel c$ (0.6, 1.8 and 4.7 eV for $\vec{E} \parallel b$), respectively, above the core absorption threshold. Using the band structure calculation by Valiukonis *et al* [10], they assigned the structures to the transition to the first conduction band doublet, of rather parallel bands, in the Z → U direction of the BZ.

In our calculation, the a–a′ structure relies on the transition from the core $3d_{5/2}$ and Se $3d_{3/2}$ levels to the A–B peak in the conduction band of the DOS. Our assignations for the b–b′ and the c structures can be seen in figure 7. Our b–b′ and c structures are 1.23 and 3.95 eV from a–a′, respectively, which is in excellent agreement with the 1.20 and 4.00 eV measured in [14].

3.2. Optical properties

From our electronic structure calculations, we determine the imaginary part of the complex dielectric function $\varepsilon_2(\omega)$ integrating in k-space (by the standard tetrahedron method [45]). The general expression for the complex dielectric tensor is [46]

$$\varepsilon_2(\omega)_{\alpha\beta} = \frac{4\pi^2 e^2}{m^2\omega^2}\sum_{i,f}\int \langle f|p_\alpha|i\rangle\langle i|p_\beta|f\rangle W_i(1-W_f)\delta(E_f - E_i - \hbar\omega)\mathrm{d}^3k \tag{1}$$

where $\langle f|p_\alpha|i\rangle$ and $\langle f|p_\beta|i\rangle$ are the dipole matrix elements corresponding to the α and β directions of the crystal (x, y or z), and f and i, are the final and initial states, respectively, W_n and E_n are the Fermi distribution function and electron energy for the nth state, respectively. The real part of the diagonal dielectric functions is computed from $\varepsilon_2(\omega)$ using the Kramers–Kronig relations in the form

$$\varepsilon_1(\omega)_{\alpha\alpha} = 1 + \frac{2}{\pi}P\int_0^\infty \frac{\omega'\varepsilon_2(\omega')_{\alpha\alpha}}{\omega'^2 - \omega^2}\mathrm{d}\omega' \tag{2}$$

where P means the principal value of the integral.

In order to give a complete discussion of the optical spectra of GeSe, we also studied the real and imaginary parts of the complex refraction index $\widetilde{n}(\omega)_{\alpha\alpha} = n(\omega)_{\alpha\alpha} + \mathrm{i}k(\omega)_{\alpha\alpha}$, where $n(\omega)$ is the ordinary refraction index and $k(\omega)$ is the coefficient of extinction, obtained from $(\widetilde{n}(\omega)_{\alpha\alpha})^2 = \varepsilon_1(\omega)_{\alpha\alpha} + \mathrm{i}\varepsilon_2(\omega)_{\alpha\alpha}$. Finally, we computed the coefficient of absorption $\alpha(\omega)$ as

$$\alpha(\omega)_{\alpha\alpha} = \frac{2\omega}{c}\left(\frac{-\mathrm{Re}(\varepsilon(\omega)_{\alpha\alpha}) + |\varepsilon(\omega)_{\alpha\alpha}|}{2}\right)^{1/2} \tag{3}$$

and the reflectivity $R(\omega)$ as

$$R(\omega)_{\alpha\alpha} = \left|\frac{1-\tilde{n}\,(\omega)^*_{\alpha\alpha}}{1+\tilde{n}\,(\omega)^*_{\alpha\alpha}}\right|^2 \tag{4}$$

where $*$ means conjugate complex.

As mentioned in section 2, we have performed our calculations of the optical properties using the scissors operator (with a constant shift of 0.38 eV) as implemented in the WIEN2k optical package: a rigid shift of the imaginary part of the dielectric function is performed before the application of the Kramers–Kronig relations for the calculation of the real part of ε, and the other optical parameters.

In order to assess convergence, we have calculated ε_2 with increasingly finer meshes for the discretization of the BZ. We found that the 90-k-point calculation did not converge, while

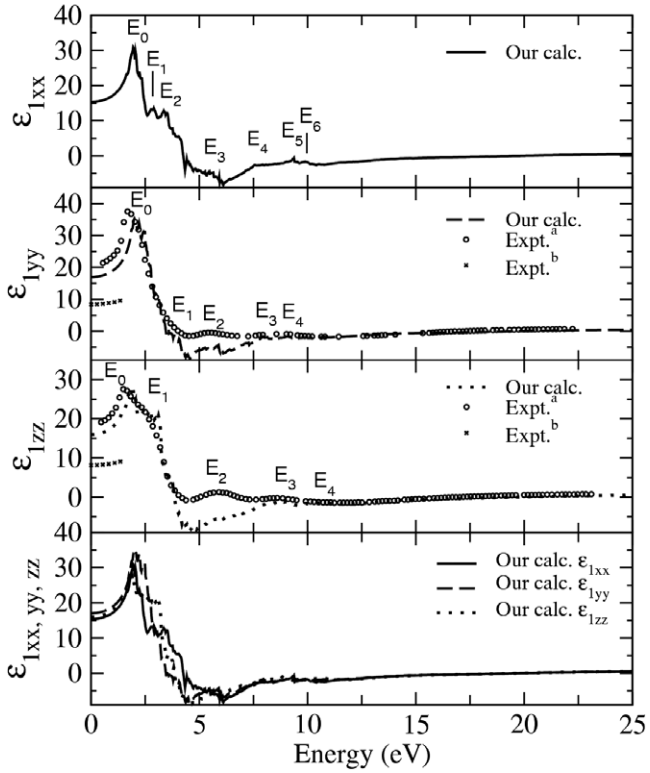

Figure 8. Calculated and experimental real part of the dielectric function [a] [9], [b] [12].

Table 3. Real part of the complex dielectric function. All $\epsilon_1(0)$ are adimensional, while the energies E_i are in eV.

	ϵ_{1xx}		ϵ_{1yy}		ϵ_{zz}	
$\epsilon_1(0)$/peaks	Our calc.	Expt	Our calc.	Expt	Our calc.	Expt
$\epsilon_1(0)$	15.37		19.02	8.40[b]	16.00	8.14[b]
E_0	1.99		2.18	1.72[a]	1.85	1.48[a]
E_1	2.87		3.81		2.53	2.53[a]
E_2	3.41		5.29	5.48[a]	5.61	5.91[a]
E_3	5.53		8.00	8.86[a]	8.83	8.62[a]
E_4	7.63		9.05		10.61	
E_5	9.37					
E_6	9.90					

[a] Reference [9].
[b] Reference [11].

the 1344- and 2520-k-point calculations coincide almost exactly. Therefore, we have assumed convergence at 2520 and calculated all the optical parameters with this sampling of the BZ.

Dielectric function. See figures 8 and 9, and tables 3 and 4. Corresponding to the largest axis, ε_{1xx} presents a sharp peak, E_0, at 1.99 and a shoulder with a double structure on it (E_1 and E_2) at around 3.11 eV. There is also a shoulder at the end of the abnormal dispersion region (E_3) and

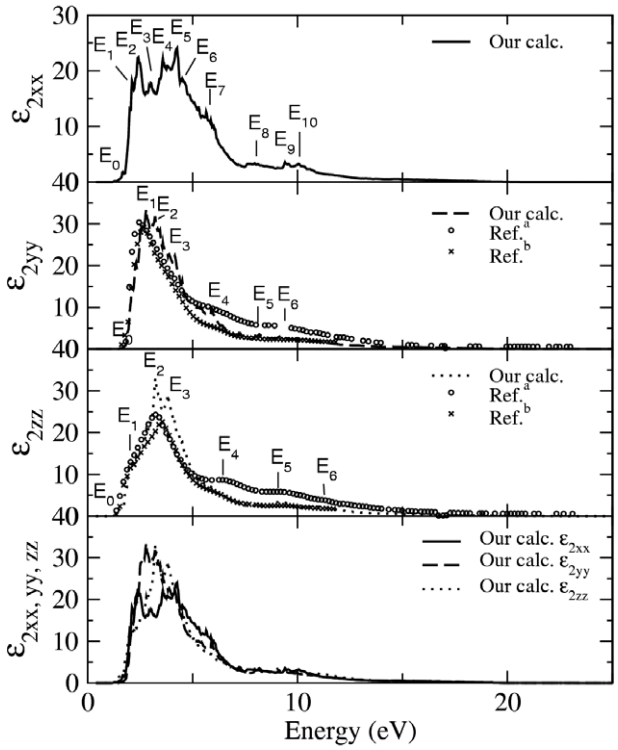

Figure 9. Calculated and experimental imaginary part of the dielectric function [a] [9], [b] [10].

three minor peaks on the rising tail of the curve (E_4–E_6) at 7.63, 9.37, and 9.90 eV, respectively. To our knowledge, no experimental curve has been reported for this spectrum. With respect to the *b*-axis, ε_{1yy}, our calculations show a peak at 2.18 eV (with a three-part fine structure on top), a slight, rather steep, shoulder (E_1) and three other structures (E_2, E_3, and E_4) similar to peaks E_3–E_5 of ε_{1xx}. The experimental curve of Eymard *et al* [9] is in good agreement with ours, specially in the energies of peaks E_2–E_4. However, it shows its maximum (E_0) 0.46 eV behind our result. Besides, it shows no structure analogous to our shoulder E_1. The *z*-axis presents a peak, E_0, at 1.85 (corresponding to the experimental [9] one at 1.48 eV) and a plateau (E_1) around 2.53 eV (which coincides with a rather shoulder-like structure of [9]). Again, our peaks E_2–E_4 are in concordance with those of Eymard *et al*, in spite of their E_2 being much more prominent than ours.

For both ε_{1yy} and ε_{1zz}, we also present Elkorashy's experimental results, which correspond to measures between 0.5 and 1.5 eV (the tail from 0.5 to 0 eV is estimated by Elkorashy from the tendency of the curve). It is clearly lower than both the results of [9] and ours. This marked difference repeats itself for the real part of the complex refraction index, *n*, and for the reflectivity. Since several experimental results plus our theoretical ones coincide among them and differ from Elkorashy's, we suggest that it might have been a systematic error included in the author's experiments.

With regards to the imaginary part of the dielectric function, ε_{2xx} presents two main, prominent structures: one of them is a single peak (E_2) at 2.42 eV, and the other is formed by two peaks (E_4 at 3.57 eV and E_5 at 4.30 eV) with a depression in between. The spectrum is completed with minor, though clearly discernible, peaks (see figure 9). In table 4, we have

Table 4. Imaginary part of the complex dielectric function. Energies are in eV. Numbers in the 'Bands' column correspond to the arrows in figures 10 and 11.

Transitions		ϵ_{2xx}			ϵ_{2yy}			ϵ_{2zz}		
DOS	Bands	Peak	Our calc.	Expt	Peak	Our calc.	Expt	Peak	Our calc.	Expt
		E_0	1.18		E_0	1.18	1.85[a]	E_0	1.18	1.40[a]
							1.56[b]			1.37[b]
							1.18[c]			1.12[c]
VBM → c_1	1	E_1	2.07					E_1	2.12	2.04[b]
v_1 → c_1	2	E_2	2.42							
v_1 → A′–B′	3				E_1	2.79	2.50[a]			
v_2 → c_1	4	E_3	3.01							
v_2 → A–B	5				E_2	3.22	3.44[b]	E_2	3.22	3.22[a]
										3.55[b]
v_2 → A′–B′	6	E_4	3.57							
v_3 → A′–B′	7							E_3	3.81	
v_2 → c_2	8	E_5	4.30		E_3	4.16				
v_4 → A–B	9	E_6	4.59							
v_3 → c_4	10	E_7	5.75							
v_6 → A′–B′	11				E_4	5.91	5.90[a]			
							6.23[b]			
v_5 → c_2	12							E_4	6.39	6.63[a]
										6.26[b]
v_7 → c_3	13	E_8	7.88		E_5	8.21				
v_7 → c_5	14							E_5	9.12	9.37[a]
										9.34[b]
v_8 → c_1		E_9	9.75		E_6	9.30	9.20[b]			
v_9 → c_1		E_{10}	10.07					E_6	11.14	11.17[b]

[a] Reference [9].
[b] Reference [10].
[c] Reference [12].

assigned to each of the peaks of ε_2 (for the three axes) a possible transition between the structures of the valence and conduction bands, labelled at the bottom DOS of figure 7. In addition, if table 1 is included in the analysis, an inference of which orbitals contribute to each peak can be made. For example, peaks E_1 of ε_{2xx} and of ε_{2zz} are assigned to the VBM → c_1 transition, where the valence band maximum (VBM) is mainly formed by p_x, p_y-Se and s-Ge, and c_1 (the first shoulder above CBM) mainly by p-Ge. Table 4 also shows that the same assignation is given to E_2 of ε_{2yy} and of ε_{2zz} (v_2 → A–B, resulting mainly from p_z, p_x, p_y-Se and from p_x,p_z-Ge, respectively), and to E_5 of ε_{2xx} and E_3 of ε_{2yy} (v_2 → c_2, resulting mainly from p_z, p_x, p_y-Se and from p_x-Ge, respectively). Although given different assignations,E_7 of ε_{2xx}, E_4 of ε_{2yy}, and E_4 of ε_{2zz} seem to correspond to each other. As to the specific origin of peaks, in figures 10 and 11 we show our bands for two different paths on the BZ, with the arrows representing possible interband transitions, originating the main E_i peaks in the optical function spectra. Both experimental results [9, 10] rise together, and for ε_{yy} they also reach together their maxima (E_1), which is slightly shifted downwards in energy with respect to our E_1. As energy increases, however, the two functions separate from each other, since the Eymard *et al* [9] result falls down more slowly than that of Valiukonis *et al* [10]. This also happens for the z-axis, for energies higher than 5 eV, approximately. Also for ε_{2zz}, the ascending edges of both the experimental and our theoretical curve coincide almost exactly; however, the experimental peaks are less strong than ours and the Valiukonis *et al* [10] peak is shifted 0.33 eV ahead in

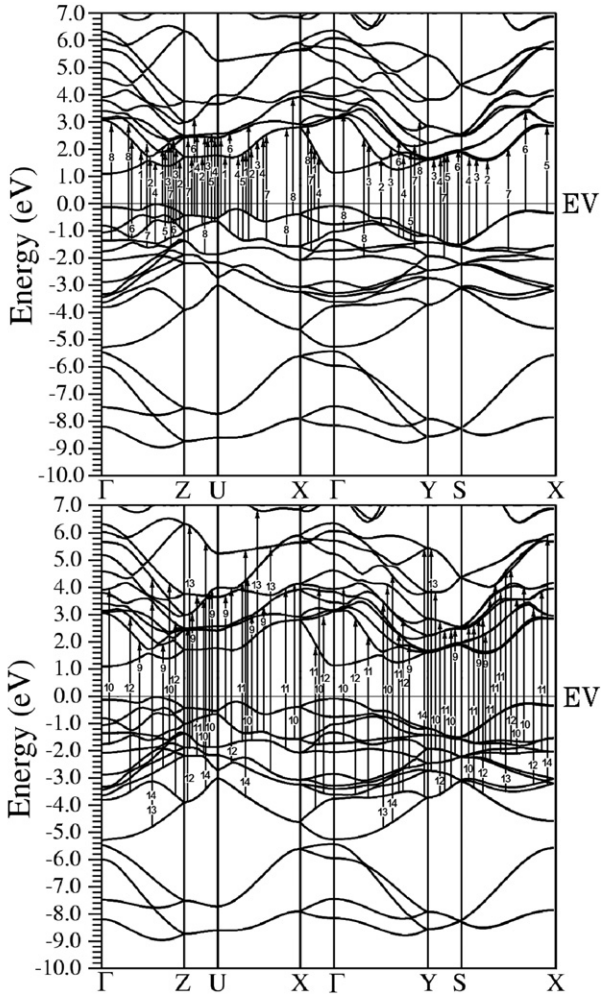

Figure 10. Band structure for the most symmetrical directions in BZ. See figure 2. The arrows represent possible interband transitions between bands originating the main peaks in the optical function spectra. For the sake of clarity, we show transitions 1–8, and 9–14 in different graphics (see table 4).

energy. The experimental results also present shoulders that might correspond to our calculated E_4 and E_5, with a greater resemblance of [10] to our results (almost exactly overlapping from around 6.5 eV up).

Complex index of refraction. With regards to n, notable features (peaks, shoulders, the refraction index for zero energy $n(0)$, and the first energy for which dispersion is null $E(n = 1)$) are extracted in table 5. Comparison with ε_1 (figure 8) shows, as was to be expected, an almost one-to-one correspondence of main features, and also as with ε_1, the experimental index of refraction of Elkorashys [12] is much lower than ours. In addition, it is interesting to notice that in the range of about 7.50–10.00 eV GeSe fluctuates around unity (i.e., $n \approx 1$) for the three axes (figure 12), so almost no dispersion is suffered by incident radiation. For this same range of incident energy, the reflectivity, figure 14, drops sensibly.

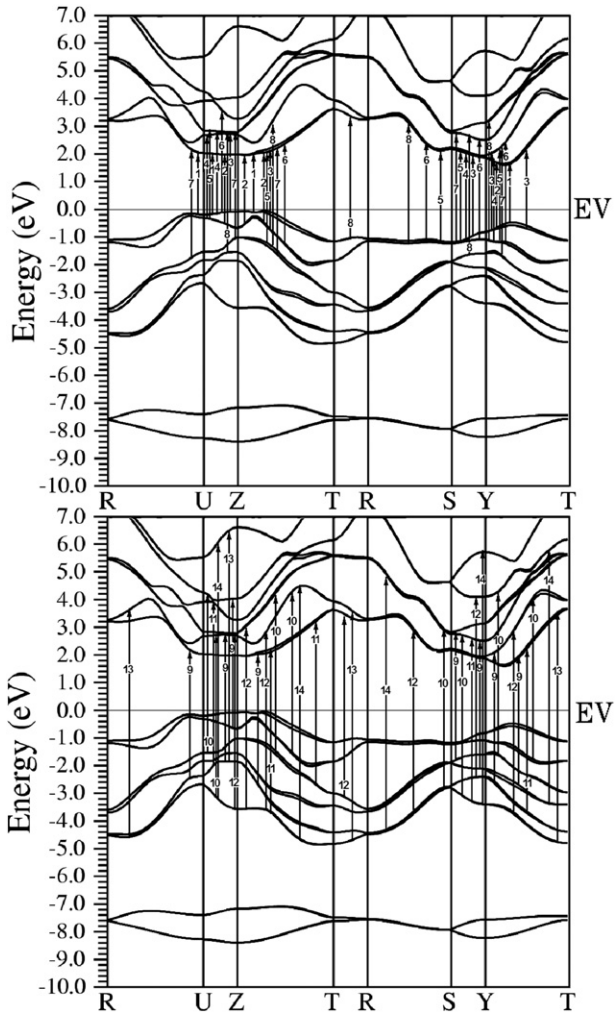

Figure 11. Band structure for the least symmetrical directions in the BZ. See figure 2. The arrows represent possible interband transitions between bands originating the main peaks in the optical function spectra. For the sake of clarity, we show transitions 1–8 and 9–14 in different graphics (see table 4).

As to the coefficient of extinction (figure 13), the notable peaks are labelled and quantitatively assessed in table 6. As to the origin of the peaks, given the close relation to those of ε_2, it is expected to be the same. We have found no experimental results to contrast against our curve; however, in table 6 we present Elkorashy's value for E_0, which he did measure (actually, derived from interference measurements) [12].

Reflectivity. With regards to this parameter (figure 14), a general look at our results shows that all three calculated reflectivities do not fall together with the experimental ones. Instead, they keep fluctuating about the value of 0.5 (i.e. 50%), only to abruptly drop at about 20.00 eV. This discrepancy could be due to imperfection of the surface polishing of the samples used by the experimentalists. As to the detailed spectra, we have labelled eight prominent structures in R_{xx}

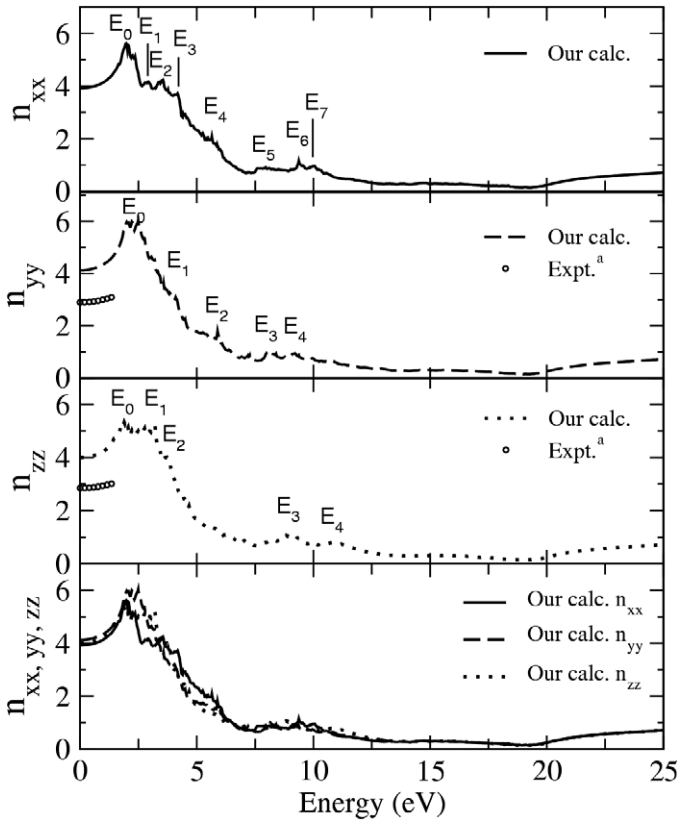

Figure 12. Calculated real part of the complex index of refraction [a] [12].

Table 5. Characteristic values and peaks of the real part of the complex index of refraction (n). All values are in eV, except for $n(o)$, which are adimensional.

	n_{xx}	n_{yy}	n_{zz}
$n_{\text{Our calc.}}(o)$, $n_{\text{Expt}}(o)$	3.92	4.13, 2.90[a]	3.99, 2.58[a]
E($n = 1$)	6.55	6.39	6.44
E_0	1.96	2.26	1.88
E_1	2.90	4.08	3.12
E_2	3.52	5.91	3.73
E_3	4.19	8.16	9.10
E_4	5.75	9.21	10.90
E_5	7.87		
E_6	9.43		
E_7	10.07		

[a] Reference [12].

and R_{yy}, and seven in R_{zz} (table 7). For R_{yy}, peaks E_1–E_3 and E_5 are in good agreement (as to their location, rather than to their amplitude) with those of the experimentalists [9, 10]; the same occurs for E_1–E_4 of R_{zz}. It is to be noticed that peaks E_0 of R_{yy} and R_{zz} only appear in the measurements of [10, 11], and not in those of [9] or in our calculations. Again, Elkorashy's [11] results differ from both the other experiments and our theoretical spectrum.

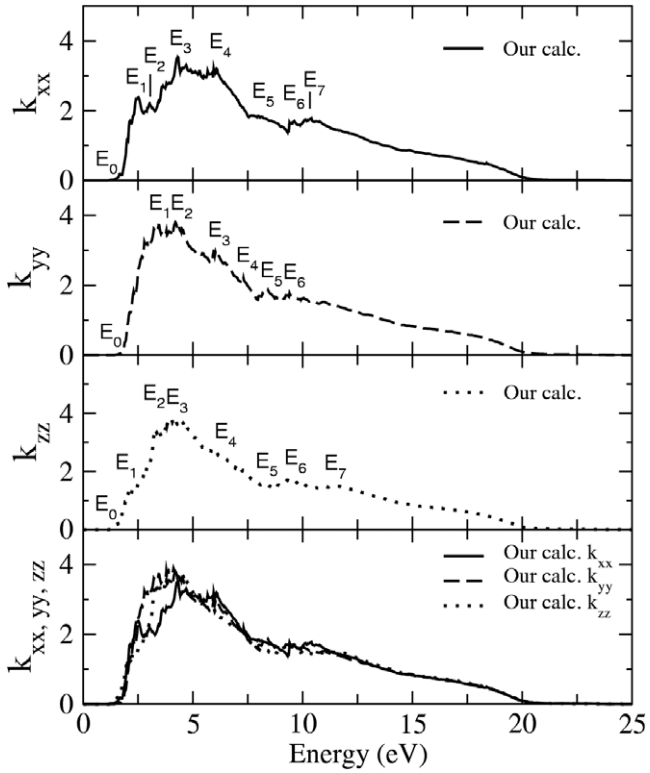

Figure 13. Calculated and experimental imaginary part of the complex index of refraction.

Table 6. Relevant peaks of the coefficient of extinction. Energies are in eV.

	k_{xx}	k_{yy}	k_{zz}
E_0	1.67	1.80	1.45
E_1	2.50	3.41	2.26
E_2	3.06	4.35	3.36
E_3	4.35	6.04	4.16
E_4	6.12	7.33	6.58
E_5	8.19	8.43	8.28
E_6	9.61	9.45	9.46
E_7	10.36		11.48

Absorption coefficient. Figure 15 and table 8 show our calculated coefficient of absorption for each of the three axes, compared with absorptions measured at 96 K for the *a* and *c* axes (in our notation), performed by Elkorashy [11]. As to the morphology, all three absorptions start at the same energy, defining an isotropic energy gap, E_0, of 1.18 eV. The absorptions for the *a* and *c* axes, α_{xx} and α_{zz}, grow together, defining a sharp edge, while α_{yy} is less steep. Thus, at the absorption edge, GeSe seems to work as a two-dimensional material. However, anisotropy among the three axes is clearly observed between 2.2 and 4.5 eV, and between 5.50 and 11.2 eV, approximately. In addition, an especial feature of α_{yy} must be mentioned: it presents a steep growth followed by a rather flat, narrow shoulder, E_1 (at 1.33 eV), that is not present in the experimental curve. This shoulder can be understood as the result of a similar structure at the

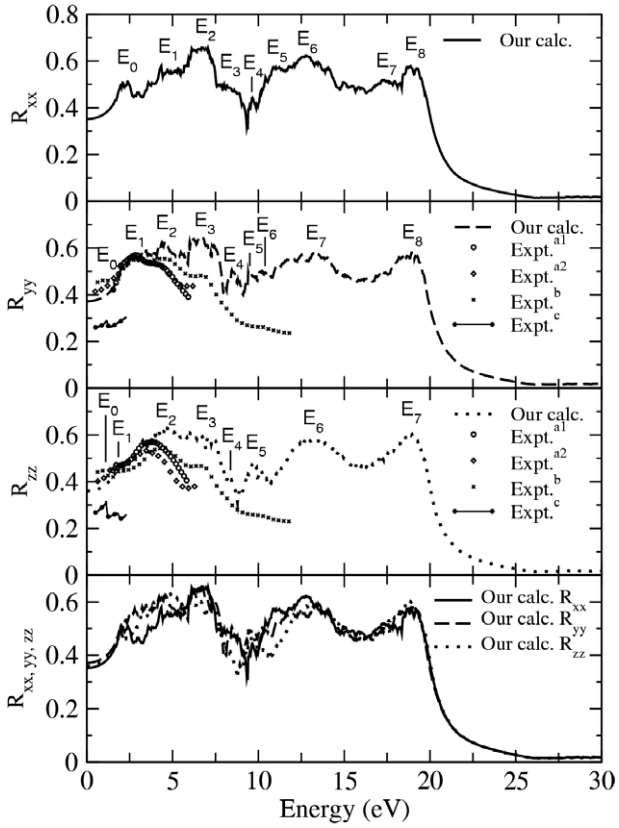

Figure 14. Calculated and experimental coefficient of reflection [a1] [9] (directly measured), [a2] [9] (calculated with the Kramers–Kronig approximation), [b] [10], [c] [11].

edge of the valence band edge of p_y-Se and p_y-Ge orbitals (figure 7): a sharp narrow structure most likely to be smoothed by thermal fluctuations. Except for this, the general behaviour of our calculations agrees with that of the experimental result of Elkorashy [11].

In all the previously discussed spectra, the spin–orbit interaction introduced subtle corrections, and figure 16 shows that for ε_2 a negligible rounding of some spiky peaks occurs due to the small changes in the band structure (commented on in section 3.1). However, paying close attention to the coefficient of absorption (figure 17), we found that from the rising edge of absorption to approximately 2 eV there are quite visible differences. For the three axes of the crystal there is observed a slight shift ($\sim$0.02 eV) of the absorption edge. In general, the absorptions with spin–orbit interaction are greater than the ones without. In particular, α_{xx} (corresponding to the largest axis of the system) presents the greatest differences. As can be derived from the expressions for the complex index of refraction and the coefficient of absorption (presented in the introductory part of this section), it follows that the difference for α is $\sim 10^5$ times the difference for k for an energy of $\sim$1 eV. This explains how neglected changes in k become noticeable in α.

The other effect that produces splitting of bands is the interaction between the double layers of atoms forming the crystal structure, as discussed for GeS by Grandke *et al* [47]. According to our calculations, this effect is stronger than the spin–orbit interaction. The effect can be seen most clearly for the two deepest bundles of bands discussed in section 3.1, the deepest

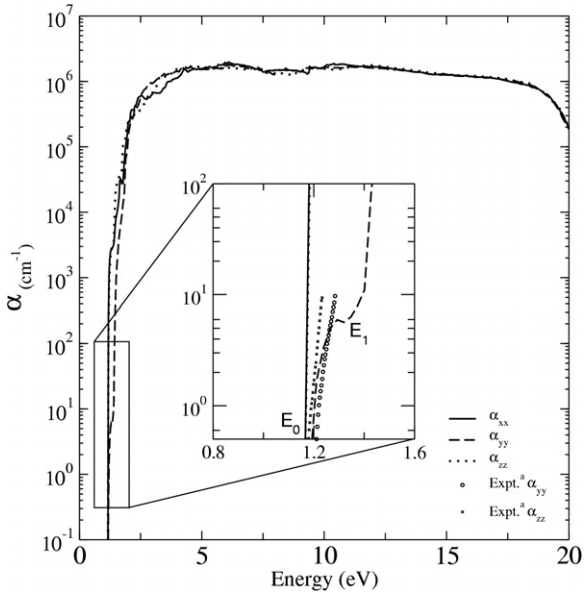

Figure 15. Calculated and experimental coefficient of absorption [a] [11].

Table 7. Experimental and calculated reflectivity at zero energy and notable peaks. All values are in eV, except for $R(o)$, which are adimensional.

	R_{xx}		R_{yy}		R_{zz}	
R(0)/Peaks	Our calc.	Expt	Our calc.	Expt	Our calc.	Expt
$R(0)$	0.35		0.37		0.36	
E_0	2.25			1.16[b]		1.10[b]
				1.16[c]		1.16[c]
E_1	4.93		2.81	2.81[a1,a2]		1.58[a2]
				2.93[b]		1.71[b]
						1.77[c]
E_2	6.61		4.51	4.54[b]	4.58	3.80[a1]
						3.48[a2]
						4.51[b]
E_3	8.35		6.77	6.77[b]	6.51	6.70[b]
E_4	9.66		8.48	8.13[b]	8.29	8.17[b]
E_5	11.05		9.54		9.70	10.24[b]
E_6	12.82		10.18	10.41[b]	13.24	
E_7	17.37		13.24		18.88	
E_8	18.95		18.88			

[a1] Reference [9] (directly measured).
[a2] Reference [9] (calculated with the Kramers–Kronig approximation).
[b] Reference [10].
[c] Reference [11].

and flattest one in the region between −14.52 and −12.37 eV, mainly corresponding to the 4s-Se level, and the following region of bands originated from the 4s-Ge level (and a minor contribution of the 4p-Se level) between −9.03 and −5.38 eV (see figures 4 and 5). With

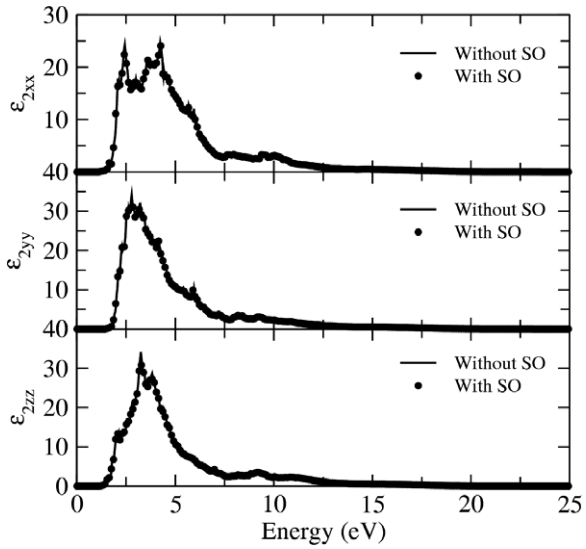

Figure 16. Imaginary part of the complex dielectric function computed with and without the inclusion of the spin–orbit interaction.

Table 8. Relevant peaks of the coefficient of absorption. Energies are in eV.

	α_{xx}		α_{yy}		α_{zz}	
Peaks	Our calc.	Expt	Our calc.	Expt	Our calc.	Expt
E_0	1.17		1.19	1.21[a]	1.17	1.18[a]
E_1			1.33			

[a] Reference [11].

respect to the region of higher energies and up to E_F, the strong hybridization of these bands prevents the effect from becoming evident. With respect to the optical spectra, the double layer interaction shows itself to be relevant in the least symmetrical regions, in the R $\rightarrow$ U, Z $\rightarrow$ T and Y $\rightarrow$ T directions of the BZ, occurring for the 4s-Ge levels (see figure 6). The splitting of these flat bands originates the peaks v_8 and v_9 in figure 7, while transitions from them to the first conduction bands give rise to the peaks about $\sim$9 and $\sim$10 eV in all optical functions (see table 4 for their exact assignation in ε_2; for clarity, their arrows (transitions) have not been shown in figures 10 and 11). The effect is also particularly visible for the real index of refraction n, with the peaks E_6 and E_7 in n_{xx}, E_4 in n_{yy} and E_3 and E_4 in n_{zz} (see figure 12 and table 5). As to the reflectivity R, the double layer interaction contributes to the peaks E_4 and E_5 in R_{xx}, E_5 and E_6 in R_{yy}, and E_5 in R_{zz} (see figure 14 and table 7). These peaks appear after a valley at about $\sim$8 eV in R, particularly well defined in R_{zz}, this depression being due to the low number of energy levels existing between peaks v_8 and v_7, as the total DOS shows in figure 7.

Final remarks. Although an overall 3D anisotropic behaviour is observed in GeSe (see the bottom of figures 8, 9, 12, 13, and 14), it is interesting to notice that anisotropy alternates with ranges of energies for which the material is actually almost isotropic. We suggest that this is an attractive feature that could be taken advantage of in the design of sensors.

With regards to disagreements among experimental results and between theoretical and experimental results, on one hand, it is well known that there are important non-rigid shifts

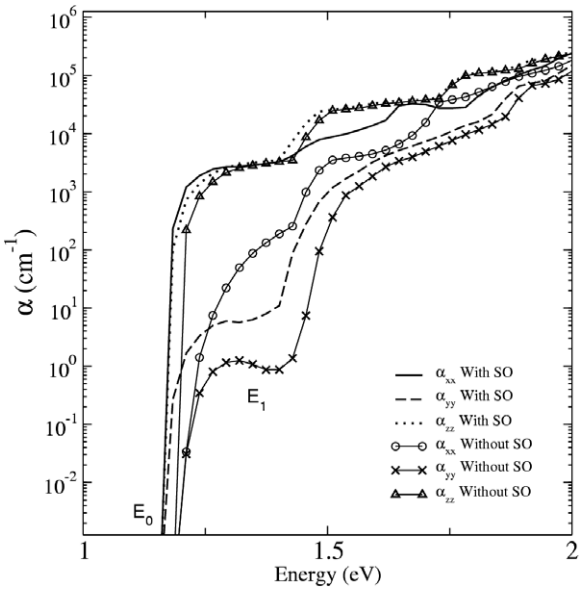

Figure 17. Detail of the calculated coefficient of absorption with and without spin–orbit interaction.

of bands in semiconductors. Thus, our application of the scissors operator is limited in its power to enhance our results. On the other, differences in amplitude might be a consequence of experimental conditions such as room temperature (it has been shown that the dielectric function of GeS falls with the increase of temperature [48], which is most likely to also happen with GeSe), finite thickness of the studied slab (which may be of importance in the reflectivity spectrum of the samples, due to backpropagation of light), and surface defects (especially in planes perpendicular to the cleavage plane) [11–13]. In fact, as with GeS [49], it is possible that the contact of GeSe samples with air produces an amorphous overlayer with a different optical response. These possibilities suggest a careful revision of the measurements of reflectivity for photonic energies above ∼4 eV, which apparently fall before they should. It is also our belief that experimental efforts should be made on the study of properties in the direction of the largest axis of GeSe, in spite of the difficulties cleavage involves. As is to be expected, experimental measurements yield smoother curves than the ones obtained numerically. In spite of this, a good agreement and characterization has been clearly achieved in this work.

4. Conclusions

We have used an *ab initio* FP-LAPW method to assess the electronic structure and optical properties of the semiconductor GeSe. Also, from our calculated conduction band and DOS, we have obtained very good agreement with the experimental core excitation spectra. We show that the spin–orbit interaction introduces minor changes in the description of the electronic structure of the material. In spite of this, we have chosen not to neglect it and have performed our complete analysis of GeSe with this interaction, and actually it turns out to be important in the detailed spectra of the coefficient of absorption α. For GeSe, we found that the LDA approximation yields results extremely similar to those of GGA. We propose the behaviour of the cationic s states as characteristic of the IV–VI materials, proving also that any theoretical

description of these materials needs to account for the s–p hybridization of the valence band in order to give a proper description of the band structure. With this electronic structure we have also thoroughly computed and characterized the optical response of GeSe, obtaining very good agreement with the available experimental data.

Acknowledgments

The authors acknowledge financial support from the Universidad Nacional de Entre Ros (UNER), and the Consejo Nacional de Investigaciones Cientficas y Tcnicas (CONICET), Argentina.

References

[1] Shi Z, Xu G, McCann P J, Fang X M, Dai N, Felix C L, Bewley W W, Vurgaftman I and Meyer J R 2000 *Appl. Phys. Lett.* **6** 3688
[2] Schwarzl T, Böberl M, Heiss W, Springholz G, Fürst J and Pascher H 2003 *Proc. GMe Forum* p 103
[3] Böberl M, Heiss W, Schwarzl T, Wiesauer K and Springholz G 2003 *Appl. Phys. Lett.* **82** 4065
[4] Schwarzl Th, Heiß W, Kocher-Oberlehner G and Springholz G 1999 *Semicond. Sci. Technol.* **14** L11
[5] Makinistian L and Albanesi E A 2006 *Phys. Rev.* B **74** 045206
[6] Shalvoy R B, Fisher G B and Stiles P J 1977 *Phys. Rev.* B **15** 2021
[7] Kemeny P C, Azoulay J, Cardona M and Ley L 1977 *Il Nuovo Cimento* **39** 709
[8] Yu L-M, Degiovanni A, Thiry P A, Ghijsen J and Caudano R 1993 *Phys. Rev.* B **47** 16222
[9] Eymard R and Otto A 1977 *Phys. Rev.* B **16** 1616
[10] Valiukonis G, Gashimzade F M, Guseinova D A, Krivaitė G, Kulibekov A M, Orudzhev G S and Šileika A 1983 *Phys. Status Solidi* b **117** 81 and references therein
[11] Elkorashy A M 1986 *Phys. Status Solidi* b **135** 707
[12] Elkorashy A M 1988 *Phys. Status Solidi* b **149** 747
[13] Elkorashy A M 1989 *Phys. Status Solidi* b **152** 249
[14] Taniguchi M, Johnson R L, Ghijsen J and Cardona M 1990 *Phys. Rev.* **42** 3634
[15] Hsueh H C and Crain J 1999 *Phys. Status Solidi* b **211** 365
[16] Onodera A, Sakamoto I and Fujii Y 1997-I *Phys. Rev.* B **56** 7935
[17] Gashimzade F M, Guliev D G, Guseinova D A and Shteinshrayber V Y 1992 *J. Phys.: Condens. Matter* **4** 1081 and references therein
[18] Koelling D D and Arbman G O 1975 *J. Phys. F: Met. Phys.* **5** 2041
[19] Andersen O K 1975 *Phys. Rev.* B **12** 3060
[20] Jepsen O, Madsen J and Andersen O K 1978 *Phys. Rev.* B **26** 2790
[21] Weinert M, Wimmer E and Freeman A J 1982 *Phys. Rev.* **26** 4571
[22] Jansen H J F and Freeman A J 1984 *Phys. Rev.* **30** 561
[23] Mattheiss L F and Hamann D R 1986 *Phys. Rev.* **33** 823
[24] Cottenier S 2002 *Density Funtional Theory and the Family of (L)APW-Methods: A Step-by-Step Introduction* (Belgium: Instituut voor Kern-en Stralingsfysica, K.U.Leuven) ISBN 90-807215-1-4, to be found at http://www.wien2k.at//reg_user/textbooks
[25] Thomas L H 1927 *Proc. Camb. Phil. Soc.* **23** 542
[26] Fermi E 1928 *Z. Phys.* **48** 73
[27] Hohenberg P and Kohn W 1964 *Phys. Rev.* **136** 864B
[28] Blaha P, Schwarz K and Luitz J 2001 Viena University of Technology
(Improved and updated version of the WIEN code, published by)
Blaha P, Schwarz K, Sorantin P and Rickey S B 1990 *Comput. Phys. Commun.* **59** 399
[29] Kohn W and Sham L J 1965 *Phys. Rev.* **140** 1133A
[30] Perdew J P and Wang Y 1992 *Phys. Rev.* B **45** 13244
[31] Perdew J P, Chevary J A, Vosko S H, Jackson K A, Pederson M R, Sing D J and Fiolhais C 1992 *Phys. Rev.* B **46** 6671
[32] Perdew J P, Burke K and Ernzerhof M 1996 *Phys. Rev. Lett.* **77** 3865
[33] Perdew J P, Burke K and Ernzerhof M 1997 *Phys. Rev. Lett.* **78** 1396
[34] Perdew J P, Kurth S, Zupan A and Blaha P 1999 *Phys. Rev.* B **82** 2544

[35] Lanoo M, Schlüter M and Sham L J 1984 *Phys. Rev.* B **32** 3890
[36] Wey S and Zunger A 1977 *Phys. Rev.* B **55** 13605
[37] Albanesi E A, Lambrecht W L and Segall B 1994 *J. Vac. Sci. Technol.* B **12** 2470
[38] Laskowski R, Christensen N E, Santi G and Ambrosch-Draxl C 2005 *Phys. Rev.* B **72** 035204
[39] Cohen M L and Chelikowsky J R 1989 *Electronic Structure and Optical Properties of Semiconductors* (*Springer Series in Solid State Sciences*) 2nd edn, vol 75, ed M Cardona (Berlin: Springer)
[40] Wei S-H and Zunger A 1997 *Phys. Rev.* B **55** 13605
[41] Albanesi E A, Okoye E C, Rodriguez C O, Peltzer y Blanca E L and Petukhov A G 2000 *Phys. Rev.* B **61** 16589
[42] Hummer K, Ambrosch-Draxl C, Bussi G, Ruini A, Caldas M J, Molinari E, Laskowski R and Christensen N E 2005 *Phys. Status Solidi* b **242** 1754
[43] Hedin L 1965 *Phys. Rev.* **139** A796
Hedin L and Lundquist S 1969 *Solid State Physics* vol 23, ed H Ehrenreich, F Seitz and D Turnbull (New York: Academic) p 1
[44] Araysetianwan F and Gunnarson G 1998 *Rep. Prog. Phys.* **61** 237
[45] Bröchl P E, Jepsen O and Andersen O K 1994 *Phys. Rev.* B **49** 16223
[46] Ambrosch-Draxl C and Abt R (Authors of the code extension for optical properties) 1998 The calculation of optical properties within WIEN97 *ICTP Lecture Notes* unpublished
[47] Grandke T and Ley L 1977 *Phys. Rev.* B **16** 832
[48] Logothetidis S, Lautenschlager P and Cardona M 1986 *Phys. Rev.* B **33** 1110
[49] Logothetidis S and Polatoglou H M 1987 *Phys. Rev.* B **36** 7491